



ORIGINAL RESEARCH ARTICLE

# A Rate- and Temperature-Dependent Thermomechanical Internal State Variable Model of the Directed Energy Deposition Process

Matthew J. Dantin and Matthew W. Priddy

Submitted: 31 May 2023 / Revised: 31 October 2023 / Accepted: 29 December 2023 / Published online: 1 February 2024

Residual stress and distortion in additively manufactured parts contribute to build failures and reduced fatigue life, which hinders process qualification and part certification in industry. Predictive models can be used to better understand thermally induced residual stresses and distortion. This study investigated the influence of two mechanical models on simulated residual stress and distortion for the directed energy deposition additive manufacturing process by comparing the thermomechanical effects of two different scanning strategies on a Ti-6Al-4V thin wall. The Evolving Microstructural Model of Inelasticity (EMMI) and an elastic–perfectly plastic (EPP) model were chosen due to their inherent differences and use in manufacturing simulations in the literature. EMMI is a physically based strain-rate- and temperature-dependent dislocation mechanics-based internal state variable plasticity model while the EPP model is a phenomenological temperature-dependent yield strength model that does not account for hardening or thermal softening. Simulation results show significant differences in the predicted stress evolution and the as-built stress contours despite similar maximum von Mises stress. In particular, EMMI demonstrated more realistic stress evolution from cyclic thermal history and large thermal gradients while EPP showed discontinuities and larger oscillations in the evolution of multiple components in the stress tensor.

**Keywords** additive manufacturing, directed energy deposition, finite element analysis, internal state variable model, residual stress, Ti-6Al-4V

## 1. Introduction

Directed energy deposition (DED) is an additive manufacturing (AM) process comprising of a laser or electron beam heat source that is coaxial with wire or blown powder feedstock, including processes such as direct metal deposition (DMD) and Laser Engineered Net Shaping (LENS) (Ref 1). Metal-based additive manufacturing (MBAM) parts with

This invited article is part of a special topical issue of the *Journal of Materials Engineering and Performance* on Residual Stress Analysis: Measurement, Effects, and Control. The issue was organized by Rajan Bhambroo, Tenneco, Inc.; Lesley Frame, University of Connecticut; Andrew Payzant, Oak Ridge National Laboratory; and James Pineault, Proto Manufacturing on behalf of the ASM Residual Stress Technical Committee.

**Matthew J. Dantin**, Department of Mechanical Engineering, Mississippi State University, 210 Carpenter Hall, Mississippi State, MS 39762; Center for Advanced Vehicular Systems (CAVS), 200 Research Blvd., Starkville, MS 39759; and Naval Surface Warfare Center Carderock Division, 9500 MacArthur Blvd., West Bethesda, MD 20817; and **Matthew W. Priddy**, Department of Mechanical Engineering, Mississippi State University, 210 Carpenter Hall, Mississippi State, MS 39762; and Center for Advanced Vehicular Systems (CAVS), 200 Research Blvd., Starkville, MS 39759. Contact e-mail: Md830@msstate.edu.

### List of Symbols

$F$	Finite strain deformation gradient
$F_\theta$	Thermal deformation gradient
$F_p$	Plastic deformation gradient
$F_d$	Volumetric deformation gradient
$F_e$	Elastic deformation gradient
$B_0$	Undeformed configuration
$B$	Deformed (current) configuration
$\tilde{B}$	First intermediate configuration
$\bar{B}$	Second intermediate configuration
$\hat{B}$	Third intermediate configuration
$C$	Cauchy–Green deformation tensor
$E$	Green–Lagrange strain tensor
$l$	Velocity gradient
$\bar{\sigma}_{eq}$	Equivalent stress (MPa)
$\bar{\kappa}_s$	Internal stress due to isotropic hardening (MPa)
$Y(\theta)$	Temperature-dependent yield strength function (MPa)
$f(\theta)$	Temperature-dependent material parameter
$\theta$	Current temperature divided by melting temperature
$\dot{\bar{\epsilon}}_s$	Rate of strain evolution due to isotropic hardening (1/s)
$H$	Hardening material constant
$R_D(\theta)$	Dynamic recovery constant
$R_s(\theta)$	Temperature-dependent static recovery constants
$Q_s(\theta)$	Temperature-dependent static recovery constants

$\dot{\beta}$	Rate of strain evolution due to kinematic hardening
$r_d(\theta)$	Temperature-dependent dynamic recovery constant
$\bar{\beta}$	Isotropic hardening (MPa)
$m_1, m_2, m_3, m_4, m_5$	Temperature-dependent yield strength function terms
<b>Abbreviations</b>	
AM	Additive manufacturing
DED	Directed energy deposition
LENS	Laser engineered net shaping
EMMI	Evolving microstructural model of inelasticity
EPP	Elastic–perfectly plastic
MBAM	Metal-based additive manufacturing
ISV	Internal state variable

significant porosity or thermally induced residual stresses can exhibit a decrease in mechanical properties, excessive distortion, reduced part quality, and poor fatigue life (Ref 2, 3). Residual stress formation is often problematic in MBAM parts because tensile residual stresses tend to form at surfaces, which can lead to decreased strength and reduced fatigue life (Ref 4). Therefore, mitigation of residual stresses during the deposition process is vital to prevent premature failure (Ref 5). Implementation of baseplate heating, prescribed interpass temperature or dwell time, and varying deposition strategies can all be used as in situ residual stress mitigation strategies while heat treatment and hot isostatic pressing are viable post-processing methods (Ref 6, 7, 8). Furthermore, the formation of unwanted residual stresses and distortion actively hinders current DED process qualification and part certification efforts (Ref 9).

Residual stresses and distortion within as-built parts are driven by the thermal history of the AM process with increased heating and cooling rates driving higher levels of distortion and residual stresses (Ref 10). Similar to welding, residual stresses are formed during the cyclic heating and subsequent cooling phases of the MBAM process (Ref 11). Previous research discussed the temperature gradient mechanism for the formation of residual stresses during MBAM processes (Ref 12). In the time that the material is heated, the feedstock rapidly expands; however, the thermal expansion is restricted by the solid previously deposited surrounding material that is at a much lower temperature. As a result, a compressive stress state is created in the deposition. As the material contracts during cooling, the material is again restricted by the plastic strain formed at the interface with the surrounding material and tensile residual stresses are formed. Thus, thermal expansion of the newly deposited layer leads to hardening and formation of residual stresses, while static recovery relieves residual stresses.

Unlike microscale or mesoscale mechanical models that include the effects of powder/wire interaction (Ref 13), porosity (Ref 14), and fluid flow in the melt pool (Ref 15), macroscale finite element-based MBAM mechanical models focus on how the temperature history drives residual stresses and distortion (Ref 16). Thus, the primary boundary conditions for finite element-based mechanical modeling are the temperature history of the build, the clamping mechanism, and the element activation scheme (Ref 17). Varying levels of macroscale

mechanical model complexity have been applied to predict the distortion and residual stresses on the part scale using the FEM: (i) inherent strain (Ref 18), (ii) J2 plasticity (Ref 19), (iii) Johnson–Cook (Ref 20), (iv) novel MBAM methods (Ref 21, 22), and (v) internal state variable (ISV) plasticity (Ref 23, 24).

The inherent strain method has been applied to various welded Ti-6Al-4V parts and found that larger, more geometrically complex parts showed more of an impact to the mechanical behavior compared to small simple structures, indicating a limitation of the inherent strain method (Ref 25). The elastic–perfectly plastic (EPP) model is a J2 approximation with an artificial stress relaxation and has been used to model the thermomechanical response of DED specimens (Ref 26). To account for the Ti-6Al-4V solid-state phase transformation strain, a stress relaxation temperature was implemented, which led to agreement with experimental distortion measurements; this finding indicated a need to develop a microstructurally motivated high-temperature constitutive model rather than relying on an aphysical stress relaxation temperature to capture the effects of static recovery and temperature-induced stress relaxation. The effects of different versions of the Johnson–Cook plasticity model on the formation of plastic strain during the laser powder bed fusion (L-PBF) of Ti-6Al-4V have been studied (Ref 20). The primary conclusion suggested that strain-rate-dependent hardening is significant in the 700–1300 °C range for L-PBF processes, and the presence of rate hardening should not be ignored when predicting the formation of residual stresses or distortion. Inspired by previous computational welding mechanics work performed by Goldak et al. (Ref 27), Ganeriwala et al. (Ref 21) implemented a material model capable of capturing the strain-rate-dependent and annealing behavior observed in MBAM with the intention of minimizing the number of constitutive parameters. This approach was novel in that the annealing effects are captured as a consequence of the viscoplasticity model that causes the stress to relax as a function of plastic strain. Furthermore, the viscoelastic model results in full stress and plastic strain relaxation while retaining the thermal strains. Their findings suggested that the proposed modeling approach could capture the residual stresses well, but were limited by not fully capturing the temperature history of the part using a lumped layer heating approach.

Physics-based ISV plasticity models that consider the effects of microstructural evolution, dislocation motion, etc., have not often been used for the prediction of residual stress and distortion associated with MBAM despite the level of mechanical accuracy they can provide in the context of rate- and temperature-dependent loading. However, researchers have used ISV models to predict the formation of residual stresses for L-PBF and the LENS process (Ref 23, 24). Promopatum et al. furthered their work with different implementations of Johnson–Cook along with the mechanical threshold stress (MTS) ISV model to examine how sensitive the prediction of residual stresses is to the choice of material model; the overall conclusion of the work was that either model could be used to predict the formation of residual stresses, but the MTS model better captured the development phase of plastic strains due to its more physically based nature. To further the notion that ISV models are better geared to capture the history and evolution of the material during processing, the Bammann–Chiesa–Johnson model (Ref 28) was implemented to track the mechanical history of a LENS build (Ref 29). Similar to Promopatum et al., they concluded that an ISV model can more accurately predict the evolution and resultant final residual stresses and strains compared to other

modeling methodologies, emphasizing that a physically motivated model is necessary for such predictions. Furthermore, Stender et al.'s conclusions are supported by measured residual strains and dislocation densities.

The purpose of this work is to present a novel ISV-based mechanical model that is equipped for capturing MBAM residual stresses and distortion. The thermal model is calibrated using with dual wave pyrometer images taken of the melt pool during the build. The rate- and temperature-dependent ISV mechanical model is calibrated using hot compression test data taken at multiple strain rates and temperatures (Ref 30). Research has demonstrated that ISV models can be used for the prediction of temperature- and strain-rate-dependent behavior in metals; thus, the results of this study can then be used to aid process parameter development to accelerate design for DED processes (Ref 31). Due to the wide range of temperatures and the rapid heating and cooling rates ( $10^6$  K/s) observed in MBAM that result in strain rates up to approximately  $4 \text{ s}^{-1}$ , a temperature- and rate-dependent ISV model was used to gain a better insight into the evolution of distortion, plastic strain, and residual stresses during a MBAM build.

## 2. Mechanical Model Background

### 2.1 The Evolving Microstructural Model of Inelasticity

The mechanical model selected for the prediction of thermally induced residual stresses and distortion of an as-built part is the evolving microstructural model of inelasticity (EMMI) (Ref 32). EMMI was developed for the prediction of the mechanical response of metals at high strain rates and temperatures. EMMI is a physically based ISV model with parameters derived from dislocation mechanics and is the successor to the Bammann–Chiesa–Johnson (BCJ) model (Ref 28). EMMI is a modification of the BCJ model with changes to the formulation of rate effects and recovery mechanisms to improve its physical basis by updating the plasticity equations to better represent dislocation mechanics. Previously, BCJ has been used to predict weld solidification cracking along with residual stresses associated with LENS™ (Ref 24, 29, 33). Although parts fabricated with MBAM do not experience the high strain rates that EMMI was intended for, the large fluctuations in temperature and thermal cycling along with resultant plastic distortion and residual stresses make EMMI an ideal candidate to model the process due to its temperature dependence and ability to capture the evolution of hardening. Typically, strain rates of up to  $4 \text{ s}^{-1}$  are observed in the MBAM process. The primary features of EMMI used in this work are: (i) temperature-dependent elastic modulus and yield strength; (ii) plasticity is described by isotropic and kinematic hardening variables; and (iii) hardening and recovery mechanisms that characterize dislocations and cell structures formed during deformation.

The finite strain deformation gradient,  $F$ , is multiplicatively decomposed into four parts for EMMI: (i) the thermal deformation gradient,  $F_\theta$ , is associated with thermal expansion, (ii) the deviatoric plastic deformation gradient,  $F_p$ , is associated with dislocation movement, (iii) the volumetric deformation gradient,  $F_d$ , is associated with damage, and (iv) the elastic recoverable deformation gradient,  $F_e$ , is associated with lattice rotation and stretch (Ref 32). Thus, the total deformation

gradient is shown in Eq 1. Damage is neglected in this implementation due to the small strain nature of MBAM.

$$F = F^e F^d F^p F^\theta \quad (\text{Eq 1})$$

The EMMI model is comprised of five configurations:

- (1) Undeformed,  $B_0$
- (2) Deformed (current),  $B$
- (3) First intermediate, defined by  $F^\theta$ , denoted as  $\tilde{B}$
- (4) Second intermediate, defined by  $F^p F^\theta$ , denoted as  $\bar{B}$
- (5) Third intermediate, defined by  $F^d F^p F^\theta$ , denoted as  $\hat{B}$

Since the components of the deformation gradient have been defined, five stretch tensors, also known as Cauchy–Green deformation tensors, can be defined in Eq 2, 3, 4, 5, and 6:

$$C = F^T F \quad (\text{Eq 2})$$

$$\tilde{C}^p = F^{pT} F^p \quad (\text{Eq 3})$$

$$C^\theta = F^{\theta T} F^\theta \quad (\text{Eq 4})$$

$$\bar{C}^e = F^{eT} F^e \quad (\text{Eq 5})$$

$$C^* = F^{*T} F^* \quad (\text{Eq 6})$$

From there, the Green–Lagrange strain tensors can be defined in Eq 7, 8, 9, 10, and 11:

$$E = \frac{1}{2}(C - 1) \quad (\text{Eq 7})$$

$$\tilde{E}^p = \frac{1}{2}(\tilde{C}^p - \bar{1}) \quad (\text{Eq 8})$$

$$E^\theta = \frac{1}{2}(C^\theta - 1) \quad (\text{Eq 9})$$

$$\bar{E}^e = \frac{1}{2}(\bar{C}^e - \bar{1}) \quad (\text{Eq 10})$$

$$E^* = \frac{1}{2}(C^* - 1) \quad (\text{Eq 11})$$

The total strain can then be decomposed:

$$\bar{E} = \bar{E}^e + \tilde{E}^p + E^\theta \quad (\text{Eq 12})$$

Using the additive property associated with the strain tensor, the relationship between the rate of deformation tensors (velocity gradient) in configurations  $\bar{B}$  and  $B$  can be defined. The velocity gradient,  $l$ , in configuration  $B$  can be computed:

$$l = \dot{F} F^{-1} = \dot{F}^e F^{e-1} + F^e \bar{L}^* F^{e-1} \quad (\text{Eq 13})$$

$$\bar{L}^* = \dot{F}^* F^{*-1} = \dot{F}^p F^{p-1} + F^p \dot{F}^\theta F^{\theta-1} F^{p-1} \quad (\text{Eq 14})$$

$$l = l^e + l^* \quad (\text{Eq 15})$$

$$l^* = F^e \bar{L}^* F^{e-1} = l^p + l^\theta \quad (\text{Eq 16})$$

where:

$$l^e = \dot{F}^e F^{e-1} \quad (\text{Eq 17})$$

$$l^p = F^e \bar{L}^p F^{e-1} \quad (\text{Eq 18})$$

$$\bar{L}^p = \dot{F}^p F^{p-1} \quad (\text{Eq 19})$$

$$l^\theta = F^e \bar{L}^\theta F^{e-1} = F^e F^p \tilde{L}^\theta F^{p-1} F^{e-1} \quad (\text{Eq 20})$$

$$\tilde{L}^\theta = \dot{F}^\theta F^{\theta-1} = \frac{\dot{F}_\theta}{F_\theta} \tilde{1} \quad (\text{Eq 21})$$

$$\bar{L}^\theta = \frac{\dot{F}_\theta}{F_\theta} \bar{1} \quad (\text{Eq 22})$$

All of the previously listed velocity gradients can be decomposed into symmetric and skew parts in their respective configuration as follows. Finally, the deformation gradient can be visualized in Fig. 1.

$$l = d + w \quad (\text{Eq 23})$$

$$d = \text{sym}(l) \quad (\text{Eq 24})$$

$$w = \text{skew}(l) \quad (\text{Eq 25})$$

The evolution of plastic strain in EMMI is represented by three primary equations: (i) the inelastic flow rule, (ii) isotropic hardening, and (iii) kinematic hardening. The inelastic flow rule is shown in Eq 26, where  $\bar{\sigma}_{\text{eq}}$  is the equivalent stress,  $\bar{\kappa}_s$  is internal stress field due to isotropic hardening,  $Y(\theta)$  is temperature-dependent yield function,  $f(\theta)$  is a temperature-dependent material parameter, and  $\theta$  is the current temperature divided by the melt temperature. Isotropic hardening in denominator represents probability that dislocations are gliding, resulting in a smoother plastic flow. The rate of strain evolution due to isotropic hardening,  $\dot{\bar{\epsilon}}_s$ , is shown in Eq 27, where  $H$  is a

hardening material constant,  $R_D(\theta)$  is a dynamic recovery constant, and  $R_s(\theta)$  and  $Q_s(\theta)$  are temperature-dependent static recovery constants. The rate of strain evolution due to kinematic hardening,  $\dot{\bar{\beta}}$ , is shown in Eq 28, where  $h$  is a hardening material constant,  $r_d(\theta)$  is a temperature-dependent dynamic recovery constant, and  $\bar{\beta}$  is isotropic hardening. The evolution of hardening is related to dislocation storage, the recovery term is based on dislocation cross slip, while the thermal (static) recovery term is based on dislocation climb via diffusion. Furthermore, the non-dimensional yield function,  $Y(\theta)$ , is shown in Eq 29, 30, and 31, where terms  $m_1$  through  $m_5$  are fit parameters. Calibration for EMMI for this implementation requires the fitting of sixteen material constants that are determined by fitting the stress response with experimental stress-strain data taken from tension tests. Calibration can be extended to other mechanical testing methods such as creep and cyclic tests. Further documentation for EMMI can be found in Marin et al. (Ref 32).

$$\dot{\bar{\epsilon}}^p = f(\theta) \left[ \sinh \left( \left\langle \frac{\bar{\sigma}_{\text{eq}}}{\bar{\kappa}_s + Y(\theta)} - 1 \right\rangle \right) \right]^n \quad (\text{Eq 26})$$

$$\dot{\bar{\epsilon}}_s = [H - R_D(\theta)\bar{\epsilon}_s]\dot{\bar{\epsilon}}^p - R_s(\theta)\bar{\epsilon}_s \sinh[Q_s(\theta)\bar{\epsilon}_s] \quad (\text{Eq 27})$$

$$\dot{\bar{\beta}} = hF^{eT} d^p F^e - r_d(\theta)\dot{\bar{\epsilon}} \sqrt{\frac{2}{3}} \|\bar{\beta}\| \bar{\beta} \quad (\text{Eq 28})$$

$$Y(\theta) = \frac{Y_1}{Y_2} \quad (\text{Eq 29})$$

$$Y_1 = m_1 [1 - \tanh(m_4(m_5 - \theta))] \quad (\text{Eq 30})$$

$$Y_2 = \left[ 1 + m_2 \exp\left(\frac{-m_3}{\theta}\right) \right]^{-1} \quad (\text{Eq 31})$$

EMMI had to be modified to account for material behavior at elevated temperatures for application specific to MBAM. Modifications include the relaxation of deviatoric stresses,

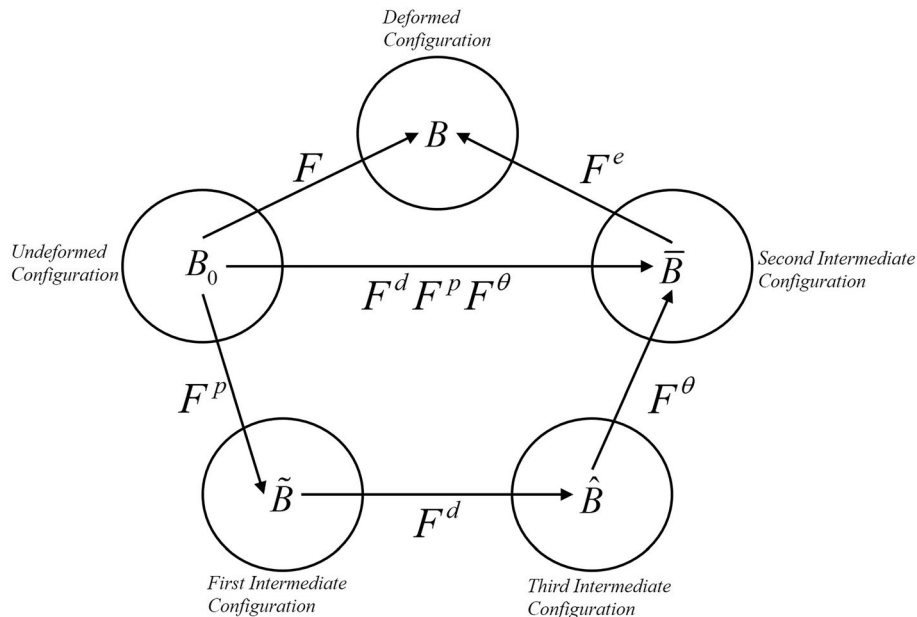


Fig. 1 The multiplicative decomposition of the deformation gradient used in EMMI

hardening state variables, and plastic strains once the element temperature exceeds 80% of the melt temperature. This assumption is based on the increased dislocation motion that occurs above this temperature causing the annihilation of work hardening, which is the result of the metal acting as a linear viscous material (Ref 34).

## 2.2 The Elastic–Perfectly Plastic (EPP) Mechanical Model

The EPP model was chosen as a comparative baseline against the EMMI model because of its use in the literature and contrast in features. EPP is based on the governing mechanical stress,  $\sigma$  equation in Eq 32, the mechanical constitutive law in Eq 33, and the total strain in Eq 34.  $C$  represents the fourth-order material stiffness tensor,  $\varepsilon$  is the total strain,  $\varepsilon_e$  is the elastic strain,  $\varepsilon_p$  is the plastic strain, and  $\varepsilon_t$  is the thermal strain. Phase transformation strain and an artificial stress relaxation temperature were neglected in this implementation. However, the initial temperature of the activated elements was set to the melting temperature to ensure that they were in a stress-free state before following the prescribed temperature history from the thermal analysis. The required mechanical inputs to run the EPP model in this formulation are temperature-dependent: elastic modulus, yield strength, and coefficient of thermal expansion.

$$\nabla \cdot \sigma = 0 \quad (\text{Eq 32})$$

$$\sigma = C\varepsilon_e \quad (\text{Eq 33})$$

$$\varepsilon = \varepsilon_e + \varepsilon_p + \varepsilon_t \quad (\text{Eq 34})$$

## 3. Thermomechanical Modeling Methodology

### 3.1 Thermomechanical Modeling Framework

A sequentially coupled thermomechanical modeling approach was used to model the AM process and resultant mechanical response. The EMMI model was implemented in a Fortran user material subroutine (UMAT) and read into ABAQUS, while the EPP model used the built-in ABAQUS implementation. The thermal analysis was run in its entirety and the temperature at each node was passed into the mechanical analysis at each time increment. At the beginning of each time increment, the deformation gradient is passed from ABAQUS to the UMAT, where it is decomposed into three

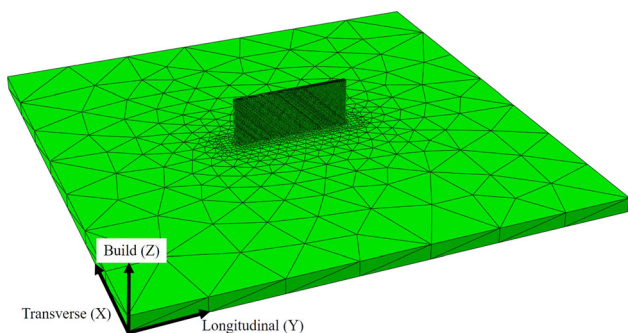


**Fig. 2** Representative finite element analysis mesh of the double-track thin wall

parts: thermal, elastic, and plastic. Then, the multiplicatively decomposed deformation gradient is used to determine the stresses and strains. Finally, the internal state variables are updated. Lastly, ABAQUS performs a check to ensure that equilibrium is maintained before proceeding to the next increment; if equilibrium is not met in a user defined number of iterations, the analysis stops.

The finite element mesh used to model the double-track thin wall is visualized in Fig. 2. A total of 433,440 continuum hexahedral (C3D8/DC3D8) elements were used to model the thin wall, while a combined total of 39,862 continuum hexahedral and continuum tetrahedral were used to model the substrate. In the thin wall, the element size was  $0.083 \times 0.083 \times 0.083$  mm with an aspect ratio of 1. Other than the temperature history from the thermal model, the only boundary condition applied to the mechanical model is the fixing of the nodes on the bottom of the substrate in each direction to account for the clamping mechanism in the LENS process.

### 3.2 Thermal Modeling Methodology

The parameters from the validated thermal model in previous work are used in the formulation of the double-track thin wall thermal model (Ref 35). The process parameters used for the build are listed in Table 1. Two different thermal histories were generated with a unidirectional and a bidirectional scanning strategy. To showcase the differences in thermal history, the temperature at a node at the end of the first deposition track is plotted in Fig. 3. The initial temperature for these simulations was 25 °C. The nodal coordinates are (50.25, 62.00, 3.675 mm) relative to the origin shown in Fig. 2. Although the observed temperatures are the same at the first two peaks above 800 °C, they begin to deviate due to the differing scanning strategies. This difference will contribute to differing thermal expansion at this node.

### 3.3 Mechanical Model Calibration

To calibrate EMMI for Ti-6Al-4V, a single-point simulator was used to iterate model parameters and compare the response to experimentally gathered data. For this study, the model parameters were calibrated to hot compression data digitized from Babu et al. (Ref 36). The range of temperatures used in the calibration process varied from 20 to 800 °C, while the strain rates range from 0.001 to 1.0 s<sup>-1</sup>. Physical mechanical properties of Ti-6Al-4V used as inputs in the EMMI model are shown in Table 2. The initial step of the calibration procedure involves the fitting of the temperature-dependent yield function at quasi-static strain rate; results of this fitting procedure are shown in Fig. 4 and Table 3. The predicted

**Table 1** Thin wall builds machine process parameters

Parameter	Value
Scanning strategy	Unidirectional & Bidirectional
Laser power, W	290
Scanning speed, mm/s	16.933
Layer height, mm	0.5
Layer width, mm	0.5
Number of layers	20
Dwell time, s	0.7

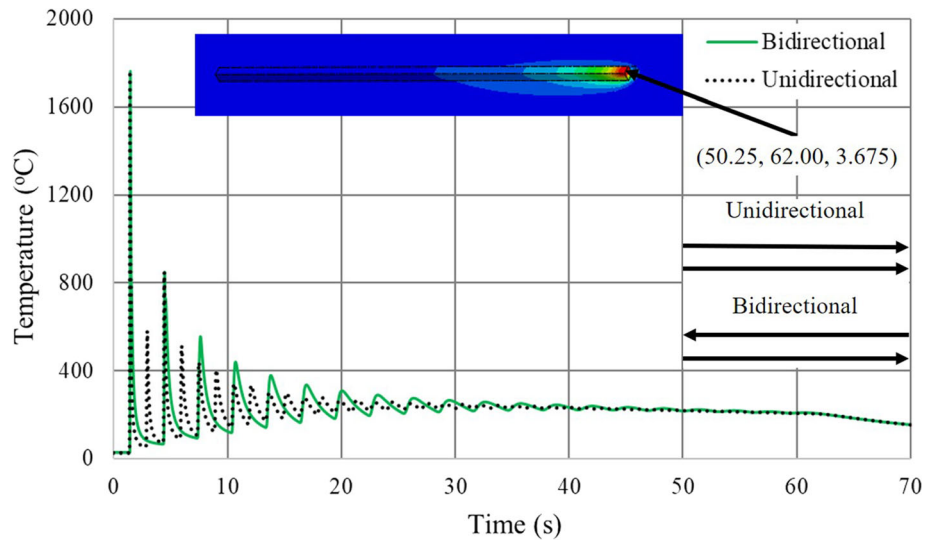


**Fig. 3** Temperature history at node of interest. The node of interest is located at the end of the first deposition track on layer one. After this point, the deposition strategy changes, as shown in the schematic

**Table 2** Ti-6Al-4V material parameters (Ref 40-42)

Property	Variable	Value	Units
Young's modulus (room temperature)	$E$	114	GPa
Poisson's ratio	$\nu$	0.33	...
Bulk modulus temperature dependence	$c_{\theta K}$	- 0.36	...
Burgers vector	$b$	$3e-7$	mm
Lattice diffusion prefactor	$D_{0v}$	185	$\text{mm}^2\text{s}^{-1}$
Lattice diffusion activation energy	$Q_v$	$2.51e8$	$\text{mJ}\cdot\text{mol}^{-1}$
Melting temperature	$\theta_M$	1933	K
Coefficient of thermal expansion	$b_0$	8.6	$\mu\text{m}/\text{m } ^\circ\text{C}$
Shear modulus (room temperature)	$\mu_0$	44	GPa
Shear modulus temperature dependence	$c_{\theta\mu}$	- 1	...

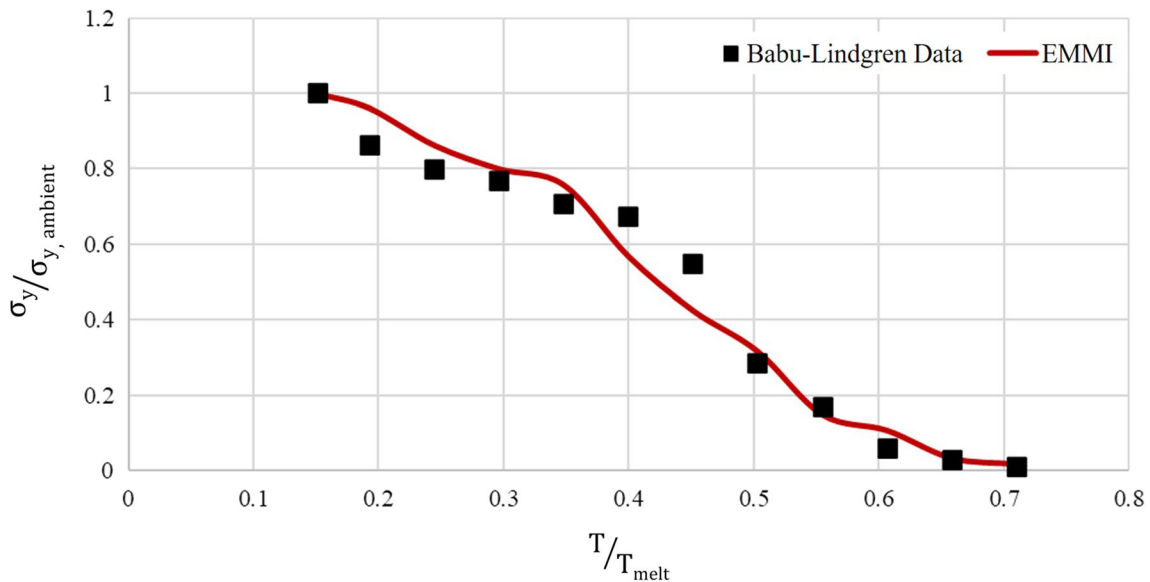


**Fig. 4** EMMI temperature-dependent normalized yield function compared to experimental data (Ref 30)

temperature-dependent yield strength follows the overall trend of the experimental, although there is slight deviation around 20% and 40% of the melt temperature. The next step in the material parameter calibration process involved the fitting of non-dimensional terms relating to material hardening and recovery variables, which are shown in Table 4.

The predicted mechanical response of both the calibrated EMMI and EPP models is compared with the experimental calibration data in Fig. 5. A significant drawback of the

**Table 3 Ti-6Al-4V temperature-dependent EMMI yield function parameters**

Parameter	Value
$m_1$	6.6
$m_2$	0.30
$m_3$	0.08
$m_4$	5.0
$m_5$	0.41

**Table 4 Ti-6Al-4V EMMI parameters**

Parameter	Description	Value
$\check{c}_1$	Flow exponent	25.2640
$\check{c}_2$	Parameter for transition rate	3.0e-10
$\check{c}_3$	Kinematic Dynamic recovery scale	5000
$\check{c}_4$	Kinematic hardening scale	0.027
$\check{c}_5$	Isotropic dynamic recovery scale	1054
$\check{c}_6$	Isotropic hardening modulus	0.01244
$\check{c}_7$	Isotropic static recovery scale	5e-7
$\check{c}_8$	Dimensionless yield parameter	0.001098

calibration process is that EPP is rate independent, and strain rates up to 4/s are observed in the DED process which could lead to significant error. However, EPP exhibits a good fit in the elastic region along with temperature-dependent the yield strength. In particular, EPP shows a more accurate fit than EMMI to the yield strength at 600 °C. Furthermore, none of the hardening behavior is captured in the EPP model, which could lead to a source of error if the associated DED processing parameters produce a part that has significant plastic deformation. For the EMMI model, the predicted stress-strain behavior captures the observed strain-rate and temperature dependency well. The hardening behavior is slightly under predicted at room temperature and over predicted at elevated temperatures, but due to the small residual strain behavior of MBAM, this set of parameters is acceptable for the prediction of residual stresses and distortion.

## 4. Results and Discussion

The first result of interest is simulated as-built von Mises stress. Figure 6 compares the von Mises stress in the as-built double-track thin walls for both scanning strategies and mechanical models. Despite the differing scanning strategies, the von Mises stress profile is nearly identical for both cases, with more stresses observed in the upper middle section and the lower left section of the unidirectional wall for each model. Furthermore, the location of the maximum stress occurs in the same node at the bottom outer edge of the wall for each case. The maximum observed stresses were approximately 100 MPa above the quasi-static room temperature yield strength of Ti-6Al-4V, indicating a small amount of plastic deformation near

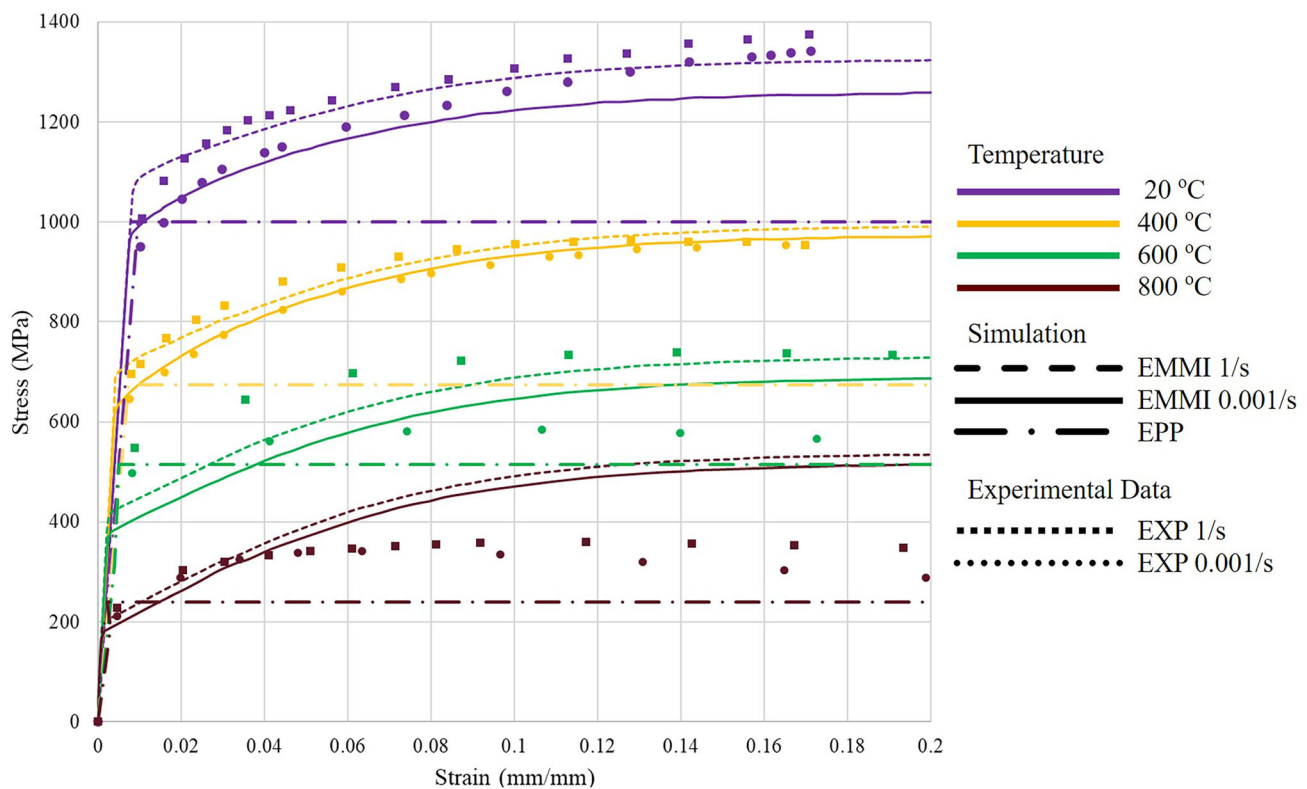


**Fig. 5** Simulated EMMI and EPP compression response compared with experimental data (Ref 30)

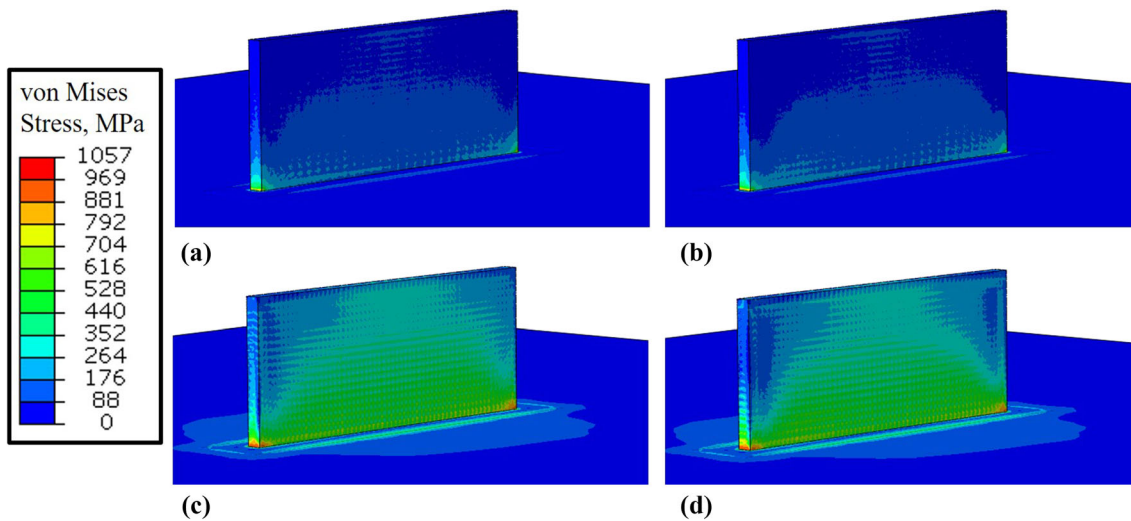


**Fig. 6** von Mises stress contours for the (a) EMMI unidirectional; (b) EMMI bidirectional; (c) EPP unidirectional; (d) EPP bidirectional

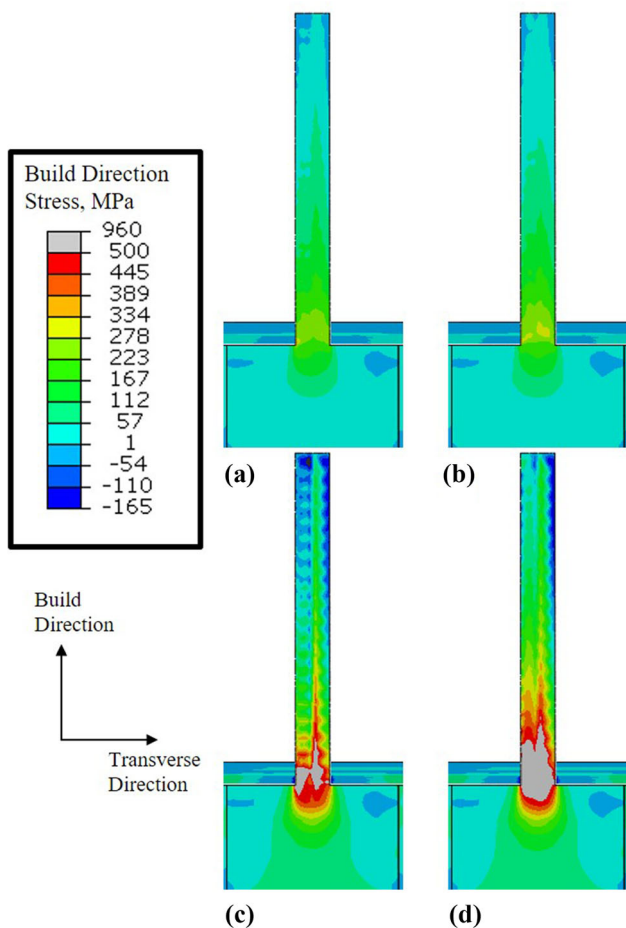


**Fig. 7** Cross section at the middle of the thin wall showing build direction residual stresses for the: (a) EMMI unidirectional; (b) EMMI bidirectional; (c) EPP unidirectional; (d) EPP bidirectional

the substrate, but these maximum residual stresses would not result in fracture of the material. Although the results using the same mechanical model are consistent, the difference in

buildup of residual stresses between the two models is significant. The EMMI simulations predict a low amount of residual stress throughout the wall with a small concentration in the outer corners. On the other hand, the EPP model predicts significant residual stresses throughout the bulk of the wall at approximately half of the room temperature yield stress.

Contour plots detailing stresses in the build direction are shown in Figs. 7 and 8. Compared to the similar von Mises stress profiles, the build direction stresses are where the stress contours begin to deviate for each model. The unidirectional scanning strategy resulted in higher magnitudes of compressive and tensile stresses compared to the bidirectional scanning strategy. Both scanning strategies resulted in tensile residual stresses at the outer free surfaces, particularly at the interface between the thin wall and the substrate, which is expected using Mercelis and Kruth's temperature gradient mechanism for the formation of residual stresses in MBAM (Ref 12). The primary differences in build direction stresses observed in Fig. 7 are the gradual buildup of residual stresses using the EMMI model, while there is a steep gradient of residual stresses observed in the EPP model. For both models, bidirectional wall shows a higher buildup of tensile residual stress at the bottom of the wall, and the unidirectional wall shows more of a compressive stress concentration in the upper middle third of the wall. The differences in build direction residual stresses for the EMMI simulations are more evident in Fig. 8, with the majority of tensile residual stresses accumulated on one half of the bidirectional wall and a more uniform buildup in the unidirectional wall.

The longitudinal stress contour for both scanning strategies is shown in Fig. 9. The primary differences in the contours occur near the outer edges of the build, where the difference in temperature history is greatest. The bulk of each wall shows a small buildup of tensile residual stresses, with compressive stresses just under zero for the bidirectional and closer to  $-100$  MPa for the unidirectional scanning strategy. The predicted contour of 0 to 200 MPa near the interface between the thin wall and the substrate is in agreement with the profile and magnitude observed in measurements by Denlinger et al. (Ref 37), meaning that EMMI has captured the evolution of longitudinal stresses in the thin walls.

The evolution of longitudinal, build direction, and von Mises stress at the node of interest from Fig. 3 is shown in



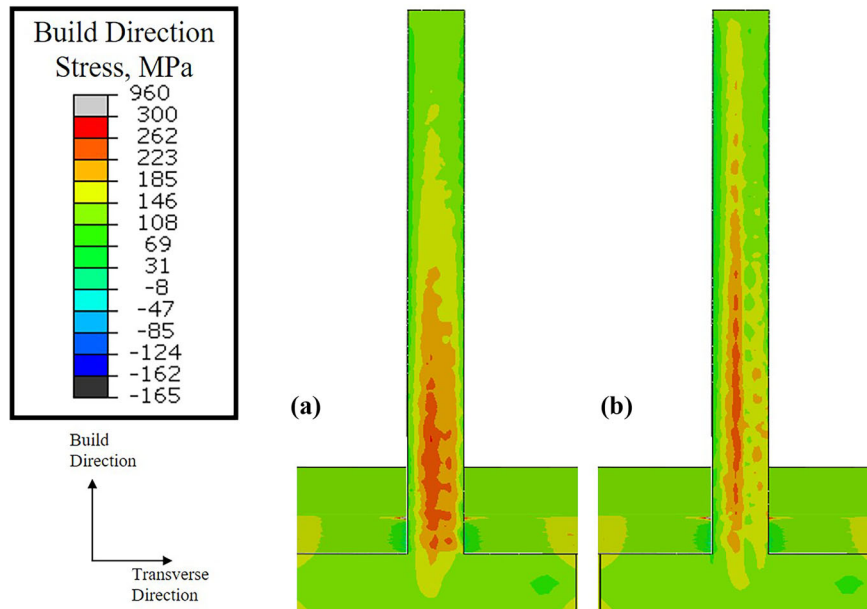


**Fig. 8** Cross section at the middle of the thin wall showing build direction residual stress comparison for the (a) EMMI unidirectional and (b) EMMI bidirectional thin wall

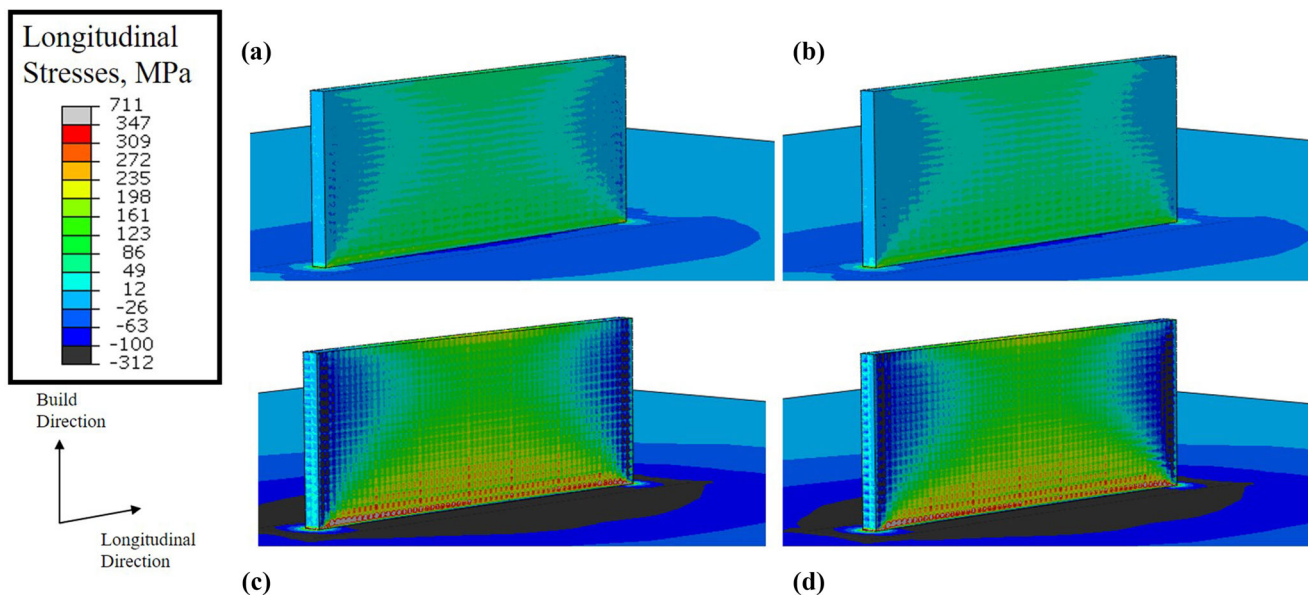


**Fig. 9** Longitudinal stress profile for the (a) EMMI unidirectional; (b) EMMI bidirectional; (c) EPP unidirectional; (d) EPP bidirectional thin walls

Figs. 10 and 11. For each case, the build direction stress is the dominant component to the stress tensor, with the von Mises stress mirroring its contour. Significant stress formation above 100 MPa does not occur until the temperature falls below 400 °C. This is significant for two reasons: (i) this indicates that overpredicting the hardening at elevated temperatures is not significantly contributing to the prediction of residual stresses because stresses at these temperatures are elastic and (ii) the majority of residual stress formation is actually occurring in a lower temperature region, due to the diminished stiffness and

strength observed at higher temperatures. This conclusion is supported by the experimental dataset that the model was calibrated to. Furthermore, the fluctuations in predicted von Mises and build direction stresses are much greater for the EPP prediction of both scanning strategies, indicating that the same amount of thermal expansion resulted in a stiffer response compared to the EMMI model.

Despite the general trend of the build direction stress dominating the stress tensor during the simulation, there are some exceptions, particularly in the EPP prediction of the

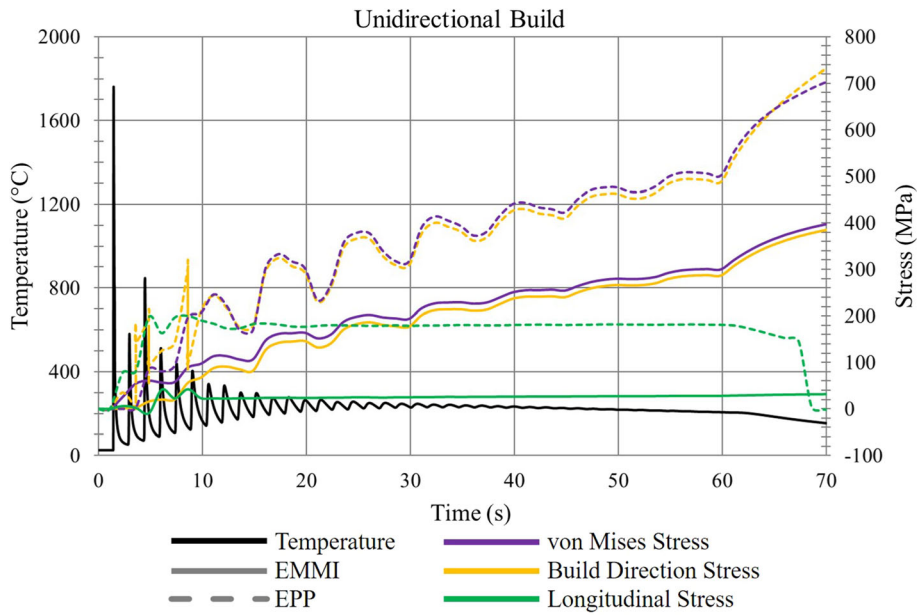


**Fig. 10** Temperature and stress evolution at the node of interest for the unidirectional scanning strategy model

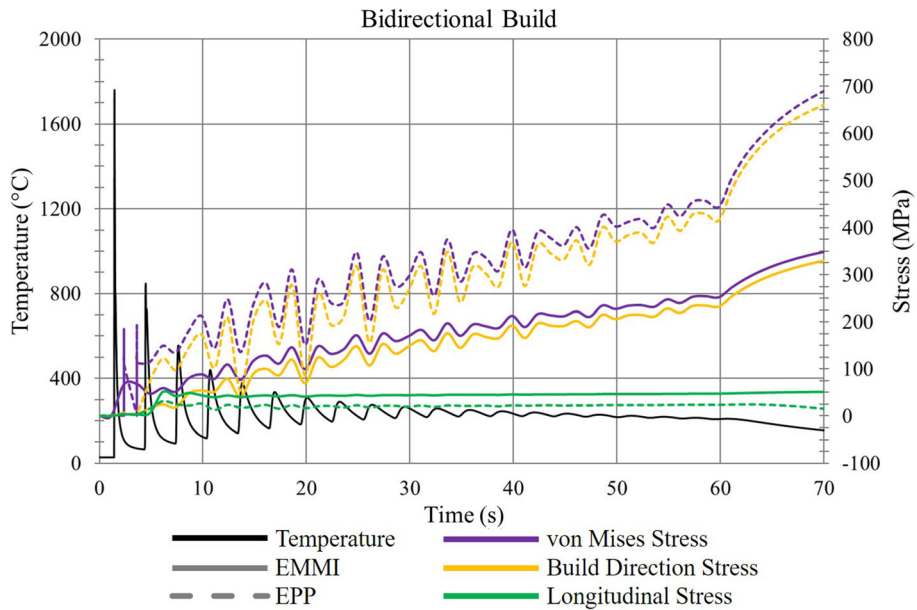


**Fig. 11** Temperature and stress evolution at the node of interest for the bidirectional scanning strategy model prediction

**Table 5 Comparison of overall maximum stresses and distortion for the unidirectional scanning strategy with the EMMI and EPP models**

Value	EMMI	EPP	Difference, %
Max von Mises stress	1,086 MPa	1,067 MPa	1.764
Max build direction stress	1,035 MPa	1,168 MPa	12.07
Max longitudinal stress	381 MPa	686 MPa	57.17
Max transverse stress	524 MPa	711 MPa	30.28
Max distortion	0.020 mm	0.062 mm	102.4

**Table 6 Comparison of overall maximum stresses and distortion for the bidirectional scanning strategy with the EMMI and EPP models**

Value	EMMI	EPP	Difference, %
Max von Mises stress	1,056 MPa	1,064 MPa	0.754
Max build direction stress	981 MPa	1,153 MPa	16.12
Max longitudinal stress	347 MPa	711 MPa	68.81
Max transverse stress	476 MPa	667 MPa	33.42
Max distortion	0.018 mm	0.060 mm	107.7

unidirectional scanning strategy. The longitudinal stress hovers around 200 MPa for the majority of the build, and then falls just below zero at the end of the build. This trend is not replicated in the EPP bidirectional prediction, which raises some concern on the reliability of an EPP model to capture the evolution of stresses during the build. However, the end result for each model is similar in numerical value for their respective scanning strategy for the longitudinal stresses, while the von Mises and build direction stresses varied by 300-350 MPa, which is approximately one-third of the Ti-6Al-4V room temperature yield stress.

Tables 5 and 6 list the maximum von Mises stress, build direction stress, longitudinal stress, transverse stress, and distortion for each scanning strategy and mechanical model. For each component of the stress tensor other than the calculated von Mises stress, the percentage difference was greater between the EPP and EMMI model for each stress component and distortion for the unidirectional scanning strategy. The observed differences between each mechanical model and scanning strategy can be attributed to the increased

stiffness of the EPP model due to the lack of static recovery compared to EMMI.

Figure 12 shows the evolution of the stress components at the location of maximum von Mises stress for the bidirectional build strategy for both the EMMI and EPP models. The locations for the maximum von Mises stress for each model were within 0.5 mm of each other at the interface between the outer surface of the wall deposit and the top of substrate. In contrast to the previous node of interest at the top of layer one, the build direction stress did not have the highest magnitude of stress in the stress tensor at the location of maximum von Mises stress for the EPP and EMMI simulations. Rather, the longitudinal stress was the highest magnitude component in the stress tensor. Furthermore, the shear stress component does not contribute much to the overall stress in the EMMI simulation until the node begins to cool under 100 °C. This is likely due to the constraint imposed by the substrate due to the location of maximum von Mises stress occurring at the interface between the substrate and the part. The increase in stress at the end could also be an artifact of the mechanical boundary conditions imposed on the bottom of the substrate,

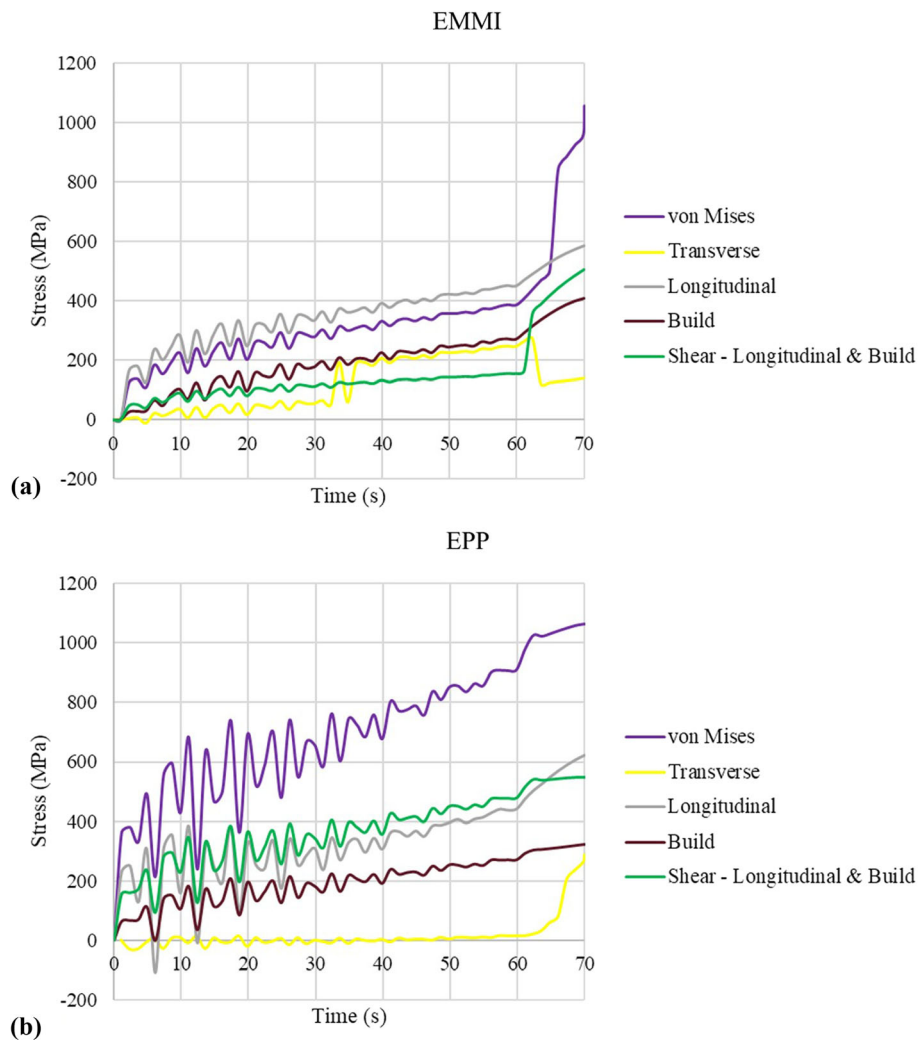


**Fig. 12** Comparison of stress evolution at location of maximum von Mises stress for the: (a) EMMI and (b) EPP models for the bidirectional scanning strategy

which fixed all of the bottom surface nodes in place. Such a constraint could artificially inflate the stress prediction at the interface between the wall and the substrate.

## 5. Conclusions

A sequentially coupled finite element thermomechanical model for the LENS process to compare the thermally induced residual stresses and distortion for as-built Ti-6Al-4V double-track thin walls using the EMMI and EPP models has been presented. Notable conclusions drawn from this work can be summarized as follows:

- When considering the calibration of the mechanical model for Ti-6Al-4V for the prediction of residual stresses and distortion, it is important to first focus on the temperature region from room temperature to 600 °C and lower, because a majority of residual stress formation occurs in this region.
- For a simple thin wall geometry, the EMMI model was able to predict different results based on scanning strategy. The unidirectional specimen was hypothesized to demonstrate higher distortion and residual stresses compared to the bidirectional scanning strategy, which it did due to the varying thermal history at the ends of the wall.
- The build direction stresses, the longitudinal stresses, and transverse stresses for the EPP model were much higher than the EMMI model. Additionally, the EMMI model better reflected the magnitude of the measured longitudinal residual stresses by Denlinger et al. (Ref 37); however, the EPP model followed the same contour shape with a higher magnitude. The stress profile at the end of the wall was likely different because the geometry in the literature was a single-track deposition.
- The general trend of the stress profile prediction, tension on the outer surfaces, and the build direction stresses dominating the stress tensor due to the thermal gradient, falls in line with trends in the literature (Ref 38).
- The predicted location of maximum stresses and distortion for each scanning strategy was the same for both the EPP and EMMI models. This is significant because if this type of thermomechanical modeling methodology is applied strictly with the intention of identifying critical stress or distortion concentrations, then a quick answer could be obtained with an EPP model.
- The difference between the maximum predicted von Mises stress between the EMMI and EPP models is within 2% for each scanning strategy. However, this maximum for the EMMI model lies at a single node for each case, indicating that further mesh refinement may be needed. The EPP model indicates a much larger area of plastic stresses at the same area compared to the EMMI model. Furthermore, the overall buildup of von Mises stresses for the EPP model is much higher than indicated by the EMMI model. This is perhaps due to the lack of recovery mechanisms present in the EPP model.
- The EPP model resulted in a much larger predicted final distortion than the EMMI model, but like the aforementioned stress contours, the patterns were the same despite the large difference in magnitude.
- The results presented in this study strengthen the notion that an EPP model produces much larger residual stresses and

distortion compared to a higher fidelity model that captures ISV evolution. These differences would likely be more drastic if the chosen DED process parameters produced a part with more distortion, as examined in other work (Ref 39).

- Ti-6Al-4V does not have a significant strain rate dependency in the strain rates relevant to powder DED (quasi-static to 4/s). Applying this comparison framework to materials with a higher strain rate dependency could yield further conclusions regarding the differences between the two modeling strategies.
- Furthermore, to better assess the differences between EMMI and EPP, more complex geometries need to be analyzed so that insight can be gained in more complex modes of conduction heat transfer.
- Finally, the difference in the runtime between the two modeling methodologies was about 2 hours, as the EMMI model ran for a total of ~ 8 hours on 60 cores, while the EPP model ran for about 10 hours on 60 cores. This difference would likely be more significant on a larger part with more elements.

## Acknowledgments

MWP would like to thank Vince Hammond of ARL for his feedback on this manuscript. MJD would like to thank Bradley Huddleston, Hamed Bakhtiarydavijani, Luke Peterson, Youssef Hammi, and Douglas Bammann of the Center for Advanced Vehicular Systems at Mississippi State University for their valuable input and troubleshooting during EMMI calibration and implementation. MJD would also like to thank J. Logan Betts for his contributions and discussion in the final stages of this manuscript. This research was sponsored by the Army Research Laboratory (ARL) and was accomplished under Cooperative Agreement Number W911NF-12-R-0011-03. The views and conclusions contained in this document are those of the authors and should not be interpreted as representing the official policies, either expressed or implied, of the Army Research Laboratory or the US Government. The US Government is authorized to reproduce and distribute reprints for Government purposes notwithstanding any copyright notation herein.

## Author Contributions

MJD was involved in conceptualization; data curation; formal analysis; investigation; methodology; validation; visualization; roles/riting—original draft. MWP helped in funding acquisition; writing—review & editing; project administration; resources; software; supervision.

## Conflict of interest

The authors declare that they have no conflict of interest.

## References

1. N. Shamsaei, A. Yadollahi, L. Bian, and S.M. Thompson, An overview of Direct Laser Deposition for Additive Manufacturing; Part II: Mechanical Behavior, Process Parameter Optimization and Control, *Addit. Manuf.*, 2015 <https://doi.org/10.1016/j.addma.2015.07.002>

2. C. Qiu, G.A. Ravi, C. Dance, A. Ranson, S. Dilworth, and M.M. Attallah, Fabrication of Large Ti-6Al-4V Structures by Direct Laser Deposition, *J. Alloys Compd.*, 2015, **629**, p 351–361. <https://doi.org/10.1016/j.jallcom.2014.12.234>
3. A. Yadollahi, M.J. Mahtabi, A. Khalili, H.R. Doude, and J.C. Newman, Fatigue Life Prediction of Additively Manufactured Material: Effects of Surface Roughness, Defect Size, and Shape, *Fatigue Fract. Eng. Mater. Struct.*, 2018, **41**, p 1602–1614. <https://doi.org/10.1111/ffe.12799>
4. B.A. Szost, S. Terzi, F. Martina, D. Boisselier, A. Prytuliak, T. Pirling, M. Hofmann, and D.J. Jarvis, A Comparative Study of Additive Manufacturing Techniques: Residual Stress and Microstructural Analysis of CLAD and WAAM Printed Ti-6Al-4V Components, *Mater. Des.*, 2016, **89**, p 559–567. <https://doi.org/10.1016/j.matdes.2015.09.115>
5. P.J. Withers, Residual Stress and its Role in Failure, *Rep. Prog. Phys.*, 2007, **70**, p 2211–2264. <https://doi.org/10.1088/0034-4885/70/12/R04>
6. K. Carpenter and A. Tabei, On Residual Stress Development, Prevention, and Compensation in Metal Additive Manufacturing, *Materials (Basel)*, 2020 <https://doi.org/10.3390/ma13020255>
7. M. Megahed, H.-W. Mindt, N. N'Dri, H. Duan, and O. Desmaison, Metal Additive-Manufacturing Process and Residual Stress Modeling, *Integr. Mater. Manuf. Innov.*, 2016 <https://doi.org/10.1186/s40192-016-0047-2>
8. G. Vastola, G. Zhang, Q.X. Pei, and Y.W. Zhang, Controlling of Residual Stress in Additive Manufacturing of Ti6Al4V by Finite Element Modeling, *Addit. Manuf.*, 2016, **12**, p 231–239. <https://doi.org/10.1016/j.addma.2016.05.010>
9. W.E. Frazier, Metal Additive Manufacturing: A Review, *J. Mater. Eng. Perform.*, 2014, **23**, p 1917–1928. <https://doi.org/10.1007/s11665-014-0958-z>
10. A.S. Wu, D.W. Brown, M. Kumar, G.F. Gallegos, and W.E. King, An Experimental Investigation into Additive Manufacturing-Induced Residual Stresses in 316L Stainless Steel, *Metall. Mater. Trans. A Phys. Metall. Mater. Sci.*, 2014, **45**, p 6260–6270. <https://doi.org/10.1007/s11661-014-2549-x>
11. N. Shamsaei, A. Yadollahi, L. Bian, and S.M. Thompson, An Overview of Direct Laser Deposition for Additive Manufacturing; Part II: Mechanical Behavior, Process Parameter Optimization and Control, *Addit. Manuf.*, 2015, **8**, p 12–35. <https://doi.org/10.1016/j.addma.2015.07.002>
12. P. Mercelis and J.P. Kruth, Residual Stresses in Selective Laser Sintering and Selective Laser Melting, *Rapid Prototyp. J.*, 2006, **12**, p 254–265. <https://doi.org/10.1108/13552540610707013>
13. M.J. Matthews, G. Guss, S.A. Khairallah, A.M. Rubenchik, P.J. Depond, and W.E. King, Denaturation of Metal Powder Layers in Laser Powder Bed Fusion Processes, *Acta Mater.*, 2016, **114**, p 33–42. <https://doi.org/10.1016/j.actamat.2016.05.017>
14. C. Teng, D. Pal, H. Gong, K. Zeng, K. Briggs, N. Patil, and B. Stucker, A Review of Defect Modeling in Laser Material Processing, *Addit. Manuf.*, 2017, **14**, p 137–147. <https://doi.org/10.1016/j.addma.2016.10.009>
15. M. Masoomi, J.W. Pegues, S.M. Thompson, and N. Shamsaei, A Numerical and Experimental Investigation of Convective Heat Transfer during Laser-Powder Bed Fusion, *Addit. Manuf.*, 2018, **22**, p 729–745. <https://doi.org/10.1016/j.addma.2018.06.021>
16. S.M. Hashemi, S. Parvizi, H. Baghbanijavid, T. Alvin, L. Tan, M. Nematollahi, A. Ramazani, and N.X. Fang, Computational Modelling of Process – Structure – Property – Performance Relationships in Metal Additive Manufacturing: A Review, *Int. Mater. Rev.*, 2021 <https://doi.org/10.1080/09506608.2020.1868889>
17. M.M. Francois, A. Sun, W.E. King, N.J. Henson, D. Tourret, C.A. Bronkhorst, N.N. Carlson, C.K. Newman, T. Haut, J. Bakosi, J.W. Gibbs, V. Livescu, S.A. Vander Wiel, A.J. Clarke, M.W. Schraad, T. Blacker, H. Lim, T. Rodgers, S. Owen, F. Abdeljawad, J. Madison, A.T. Anderson, J. Fattebert, R.M. Ferencz, N.E. Hodge, S.A. Khairallah, and O. Walton, Modeling of Additive Manufacturing Processes for Metals: Challenges and Opportunities, *Curr. Opin. Solid State Mater. Sci.*, 2017, **21**, p 1–9. <https://doi.org/10.1016/j.cossms.2016.12.001>
18. X. Liang, L. Cheng, Q. Chen, Q. Yang, and A.C. To, A Modified Method for Estimating Inherent Strains From Detailed Process Simulation for Fast Residual Distortion Prediction of Single-Walled Structures Fabricated by Directed Energy Deposition, *Addit. Manuf.*, 2018, **23**, p 471–486. <https://doi.org/10.1016/j.addma.2018.08.029>
19. E.R. Denlinger, *Thermo-Mechanical Modeling of Large Electron Beam Builds*, 1st ed. Elsevier Inc., Amsterdam, 2017. <https://doi.org/10.1016/B978-0-12-811820-7.00012-4>
20. P. Promopattum and A.D. Rollett, Influence of Material Constitutive Models on Thermomechanical Behaviors in the Laser Powder Bed Fusion of Ti-6Al-4V, *Addit. Manuf.*, 2020 <https://doi.org/10.1016/j.addma.2020.101680>
21. R.K. Ganeriwala, M. Strantz, W.E. King, B. Clausen, T.Q. Phan, L.E. Levine, D.W. Brown, and N.E. Hodge, Evaluation of a Thermomechanical Model for Prediction of Residual Stress during Laser Powder Bed Fusion of Ti-6Al-4V, *Addit. Manuf.*, 2019, **27**, p 489–502. <https://doi.org/10.1016/j.addma.2019.03.034>
22. A. Nycz, Y. Lee, M. Noakes, D. Ankit, C. Masuo, S. Simunovic, J. Bunn, L. Love, V. Oancea, A. Payzant, and C.M. Fancher, Effective Residual Stress Prediction Validated with Neutron Diffraction Method for Metal Large-Scale Additive Manufacturing, *Mater. Des.*, 2021, **205**, p 109751. <https://doi.org/10.1016/j.matdes.2021.109751>
23. P. Promopattum and A.D. Rollett, Physics-Based and Phenomenological Plasticity Models for Thermomechanical Simulation in Laser Powder Bed Fusion Additive Manufacturing: A Comprehensive Numerical Comparison, *Mater. Des.*, 2021, **204**, p 109658. <https://doi.org/10.1016/j.matdes.2021.109658>
24. K.L. Johnson, T.M. Rodgers, O.D. Underwood, J.D. Madison, K.R. Ford, S.R. Whetten, D.J. Dagle, and J.E. Bishop, Simulation and Experimental Comparison of the Thermo-Mechanical History and 3D Microstructure Evolution of 304L Stainless Steel Tubes Manufactured Using LENS, *Comput. Mech.*, 2018, **61**, p 559–574. <https://doi.org/10.1007/s00466-017-1516-y>
25. X. Lu, X. Lin, M. Chiumenti, M. Cervera, Y. Hu, X. Ji, L. Ma, H. Yang, and W. Huang, Residual Stress and Distortion of Rectangular and S-Shaped Ti-6Al-4V Parts by Directed Energy Deposition: Modelling and Experimental Calibration, *Addit. Manuf.*, 2019, **26**, p 166–179. <https://doi.org/10.1016/j.addma.2019.02.001>
26. E.R. Denlinger and P. Michaleris, Effect of Stress Relaxation on Distortion in Additive Manufacturing Process Modeling, *Addit. Manuf.*, 2016 <https://doi.org/10.1016/j.addma.2016.06.011>
27. J. Goldak and M. Akhlagi, *Computational Welding Mechanics*, Springer, Berlin, 2005
28. D.J. Bammann, An Internal Variable Model of Viscoplasticity, *Int. J. Eng. Sci.*, 1984, **22**, p 1041–1053.
29. M.E. Stender, L.L. Beghini, J.D. Sugar, M.G. Veilleux, S.R. Subia, T.R. Smith, C.W.S. Marchi, A.A. Brown, and D.J. Dagle, A Thermal-Mechanical Finite Element Workflow for Directed Energy Deposition Additive Manufacturing Process Modeling, *Addit. Manuf.*, 2018, **21**, p 556–566. <https://doi.org/10.1016/j.addma.2018.04.012>
30. B. Babu, A. Lundbäck, and L.-E. Lindgren, Simulation of Ti-6Al-4V Additive Manufacturing Using Coupled Physically Based Flow Stress and Metallurgical Model, *Materials (Basel)*, 2019, **12**, p 3844. <https://doi.org/10.3390/ma12233844>
31. M.F. Horstemeyer and D.J. Bammann, Historical Review of Internal State Variable Theory for Inelasticity, *Int. J. Plast.*, 2010, **26**, p 1310–1334. <https://doi.org/10.1016/j.ijplas.2010.06.005>
32. E.B. Marin, D.J. Bammann, R.A. Regueiro, and G.C. Johnson, On the Formulation, Parameter Identification and Numerical Integration of the EMMI Model: Plasticity and Isotropic Damage (2006). <https://www.osti.gov/biblio/883488>
33. J.J. Dike, J.A. Brooks, D.J. Bammann, M. Li, J.S. Krafcik, and N.Y.C. Yang, Predicting Weld Solidification Cracking Using Damage Mechanics -LDRD Summary Report (1997)
34. J.A. Goldak and M. Akhlagi, *Computational Welding Mechanics*, Springer US, New York, 2005
35. M.J. Dantin, W.M. Furr, and M.W. Priddy, Toward a Physical Basis for a Predictive Finite Element Thermal Model of the LENS™ Process Leveraging Dual-Wavelength Pyrometer Datasets, *Integr. Mater. Manuf. Innov.*, 2022, **11**, p 407–417. <https://doi.org/10.1007/s40192-022-00271-6>
36. B. Babu and L.E. Lindgren, Dislocation Density Based Model for Plastic Deformation and Globularization of Ti-6Al-4V, *Int. J. Plast.*, 2013, **50**, p 94–108. <https://doi.org/10.1016/j.ijplas.2013.04.003>
37. E.R. Denlinger, J.C. Heigel, and P. Michaleris, Residual Stress and Distortion Modeling of Electron Beam Direct Manufacturing Ti-6Al-4V, *Proc. Inst. Mech. Eng. Part B J. Eng. Manuf.*, 2015, **229**, p 1803–1813. <https://doi.org/10.1177/0954405414539494>

38. C. Li, Z.Y. Liu, X.Y. Fang, and Y.B. Guo, Residual Stress in Metal Additive Manufacturing, *Procedia CIRP*, 2018, **71**, p 348–353. <https://doi.org/10.1016/j.procir.2018.05.039>
39. M.J. Dantin, Thermomechanical Modeling Predictions of the Directed Energy Deposition Process Using a Dislocation Mechanics Based Internal State Variable Model, Mississippi State University (2021)
40. X. Xu and P. Nash, Sintering Mechanisms of Armstrong Prealloyed Ti-6Al-4V Powders, *Mater. Sci. Eng. A*, 2014, **607**, p 409–416. <https://doi.org/10.1016/j.msea.2014.03.045>
41. E. Alabort, P. Kontis, D. Barba, K. Dragnevski, and R.C. Reed, On the Mechanisms of Superplasticity in Ti-6Al-4V, *Acta Mater.*, 2016, **105**, p 449–463. <https://doi.org/10.1016/j.actamat.2015.12.003>
42. K.C. Mills, Recommended Values of Thermophysical Properties for Selected Commercial Alloys, Woodhead Publishing Ltd., Cambridge, 2002

**Publisher's Note** Springer Nature remains neutral with regard to jurisdictional claims in published maps and institutional affiliations.

Springer Nature or its licensor (e.g. a society or other partner) holds exclusive rights to this article under a publishing agreement with the author(s) or other rightsholder(s); author self-archiving of the accepted manuscript version of this article is solely governed by the terms of such publishing agreement and applicable law.